# Synthesis of $Fe_2O_3$ nanoparticle-decorated N-doped reduced graphene oxide as an effective catalyst for Zn-air batteries

Peng Tan[1,2], Bin Chen[2], Haoran Xu[2], Weizi Cai[2], Wei He[2], Meng Ni[2,3,*]

1 Department of Thermal Science and Energy Engineering, University of Science and Technology of China, Hefei 230026, Anhui, China

2 Department of Building and Real Estate, The Hong Kong Polytechnic University, Hung Hom, Kowloon, Hong Kong, China

3 Environmental Energy Research Group, Research Institute for Sustainable Urban Development (RISUD), The Hong Kong Polytechnic University, Hung Hom, Kowloon, Hong Kong, China

[*]Corresponding Author, Tel: +852-27664152, E-mail: meng.ni@polyu.edu.hk (Meng Ni)

**Abstract:** The advancement of Zn-air batteries requires effective and inexpensive electrocatalysts that facilitate the oxygen reduction reaction (ORR) and evolution reaction (OER). Herein, we report an effective electrocatalyst of $Fe_2O_3$ nanoparticle-decorated N-doped reduced graphene oxide ($Fe_2O_3$/N-rGO), in which porous $Fe_2O_3$ nanoparticles of ~37 nm are anchored on the N-rGO surface uniformly. In an alkaline solution, the synthesized $Fe_2O_3$/N-rGO affords superior ORR and OER activity in comparison with $Fe_2O_3$ and N-rGO, demonstrating the reinforced synergistic effect. Moreover, it exhibits a comparable limiting current density and a higher current retention ratio in the ORR than commercial Pt/C. A Zn-air battery with $Fe_2O_3$/N-rGO delivers a peak power density of 80.1 mW $cm^{-2}$, and the energy density reaches 730.2 Wh $kg_{Zn}^{-1}$. In addition, stable voltage gaps of ~0.91 V during discharge and charge are achieved at 5 mA $cm^{-2}$, and the energy efficiency is maintained at ~60% over 120 cycles, illustrating the remarkable stability for rechargeable Zn-air batteries.

**Keywords:** $Fe_2O_3$ nanoparticles; N-doped reduced graphene oxide; electrocatalyst; Zn-air

batteries; stability

## 1. Introduction

High-performance energy conversion and storage systems are crucial for the development of electric vehicles and electronic devices.[1] Among them, increasing research interests have been given in rechargeable Zn-air batteries.[2] In this type of batteries, metallic Zn is used as the negative electrode, and its dissolution and deposition occur during discharge and charge. On the positive electrode, the corresponding reactions include the oxygen reduction reaction (ORR) and evolution reaction (OER).[3] As oxygen can be directly obtained from ambient air, the energy density is further enhanced.[4] Different from other rechargeable metal-air batteries (e.g., Li/Na-air batteries),[5,6] aqueous electrolytes can be used in Zn-air batteries instead of flammable aprotic ones, ensuring the intrinsic safety.[7] However, to make this technology commercially viable, the sluggish kinetics in the oxygen reduction and evolution is a key challenge that should be well addressed, which leads to large voltage gaps and low energy efficiency.[8] Although the use of noble metal-based materials (e.g., Pt/C and Ir/C) can effectively reduce the discharge-charge voltage gap, their high prices are the bottleneck for extensive commercialization.[9] In addition, the poor stability during long-term operation impedes their large-scale applications.[10] For proton exchange membrane fuel cells (PEMFCs) in automotive applications, it would be necessary to maintain the catalytic activity for over ~5000 h.[11] While in rechargeable Zn-air batteries, the catalyst should offer both ORR and OER activity to facilitate the discharge and charge processes, and the stability requirement may be much higher. Therefore, developing low-cost and effective catalysts toward the ORR and OER and excellent stability is essential for the advancements of Zn-air

batteries.[12]

Research attention has been paid to transition metal oxides due to their cheap price, high abundance, facile synthesis, and reasonable electrochemical activity.[13–17] Particularly, owing to the striking electrochemical activity and cost-effectiveness, Mn-, Co-, and Ni-based oxides have been extensively investigated.[18–21] However, recent investigations have indicated that iron oxides, which have been neglected for a long time, can exhibit enhanced electrochemical performance.[22–27] For example, Li et al. reported that α-$Fe_2O_3$/N-doped carbon nanotubes (CNTs) have superior ORR activity with a lower onset potential of −0.21 V (vs. Ag/AgCl) and a more efficient four-electron transfer process.[25] Chen et al. fabricated a catalyst composed of Fe-N-doped carbon foam nanosheets in which carbon-coated $Fe_2O_3$ nanoparticles are embedded. It presented a half-wave potential of 0.535 V and excellent stability through maintaining 96.3% of the initial current after operation for 20000 s.[26] Ciucci et al. fabricated $Fe_2O_3$ wrapped in P and S co-doped graphitized carbon, which delivered a potential gap of 0.86 V between achieving −3 mA $cm^{-2}$ in the ORR and 10 mA $cm^{-2}$ in the OER and a favorable catalytic durability.[27] Consequently, the promising performance of metal-air batteries was achieved using $Fe_2O_3$-based catalysts.[28–32] Li et al. synthesized $Fe_2O_3$ and NiO deposited CNTs, which overcame the drawbacks of low electrical conductivity and agglomeration. The ORR and OER activity could be comparable to commercial Pt-C/$RuO_2$ catalysts, and a Zn-air battery was able to be cycled for 900 min with the discharge voltage degradation of only 0.05 V.[33] Zhang et al. synthesized Fe/$Fe_2O_3$ nanoparticles anchored on Fe-N-doped CNTs, and the battery delivered a peak power density of 193 mW·$cm^{-2}$.[34]

Previous investigations have indicated that $Fe_2O_3$ suffers from poor electrical

conductivity. Besides, the nanoparticles are easy to aggregate, which may sacrifice the active surfaces.[28] To this end, carbon supports (e.g., carbon powder, nanotubes) with high conductivity are needed to possess high electrocatalytic activity.[28–30] Among various carbon materials, graphene is an appealing one owing to the excellent physiochemical properties, including large specific surface area, high electronic conductivity, and outstanding mechanical flexibility and stability.[35–37] Further, doping graphene with N can modify the electronic properties of the $sp^2$-hybridized carbon matrix, enhancing the electrochemical activity.[38–41] Hence, an effective strategy is to combine metal oxides with N-doped graphene, through which the electrical conductivity can be enhanced, and the nanoparticles can be well segregated. Moreover, the synthetic effects of N-doping and metal oxides can lead to significant improvements in electrochemical performance.[42]

Herein, we reported $Fe_2O_3$ nanoparticle-decorated N-doped reduced graphene oxide ($Fe_2O_3$/N-rGO) as an effective catalyst for Zn-air batteries. Porous $Fe_2O_3$ nanoparticles of ~37 nm in size are anchored on the N-rGO surface uniformly, preventing the nanoparticle aggregation and improving the electrical conductivity. In addition, the mesoporous structure decreases the routes for species transport and offers abundant reaction sites. Moreover, synergetic effects between $Fe_2O_3$ and N-rGO change the electron distribution and enhance the electrocatalytic reactions. The electrochemical properties of $Fe_2O_3$/N-rGO toward the ORR and OER were first examined in a three-electrode cell. Then, the $Fe_2O_3$/N-rGO was applied as the electrocatalyst in a Zn-air battery, and the power density and gravimetric energy density were tested. Moreover, the discharge-charge cycling stability was estimated through a pulse test at 5 mA $cm^{-2}$.

## 2. Experimental

### 2.1 Synthesis of $Fe_2O_3$/N-rGO

The synthesis of $Fe_2O_3$/N-rGO was performed using a two-step method. In the first step, $Fe_2O_3$ nanoparticles were synthesized using a chemical precipitation method.[43] 5 mmol of $Fe(NO_3)_3 \cdot 9H_2O$ was dissolved in 100 mL of distilled water at 80 $^oC$. The 2 M $NH_4OH$ solution was added dropwise until the pH value reached 11. The suspension was maintained at 80 $^oC$ under stirring for 3 h, after that the resultant precipitations were washed with distilled water, dried thoroughly, and calcined in air at 700 $^oC$ for 4 h. In the second step, $Fe_2O_3$/N-rGO was synthesized using a modified hydrothermal method.[42] Briefly, 6 mg of GO (Turing Evolutionary Tech. Co., Shenzhen) was dispersed in 60 mL of anhydrous ethanol to form a uniform suspension, and 24 mg of prepared $Fe_2O_3$ nanoparticles was added, followed by sonication for 30 min, which was then heated at 80 $^oC$ under stirring for 5 h. After cooling down naturally, 2.5 mL of $NH_4OH$ (25 wt%) was added, and the suspension was transferred into a Teflon-lined autoclave. The hydrothermal reaction was performed at 180 $^oC$ for 10 h, and the precipitates were washed thoroughly and dried at 60 $^oC$ for 12 h. For comparison, the synthesis of N-rGO was using a similar approach without the addition of $Fe_2O_3$ nanoparticles. Compared with the previous approaches using the $NH_3$ gas and high temperatures, a relatively facile approach for N-dope rGO is applied, and the particle size of $Fe_2O_3$ nanoparticles can be well controlled.[23,25]

### 2.2 Physicochemical characterization

The synthesized material was characterized by X-ray diffraction (XRD, Rigaku Smartlab) with a Cu-Kα source at 40 keV and Micro-Raman spectrophotometry (Renishaw RM 3000)

at the excitation wavelength of 514 nm to examine the composition. The morphology was observed by a high-resolution transition electron microscope (TEM, JEOL 2100F). The nitrogen adsorption-desorption isotherms were got from ASAP 2020, through which the specific surface area and pore structure were obtained through Brunaure-Emmert-Teller (BET) and Barrett-Joyner-Halenda (BJH) methods, respectively. The thermogravimetric analysis (TGA) was conducted under the air atmosphere from 25 to 800 $^{o}$C using a heating rate of 10 $^{o}$C min$^{-1}$.

**2.3 Electrochemical analyses**

The electrochemical properties were first evaluated using a Solartron SI 1287 potentiostat. To prepare the working electrode, 2 mg of conductive carbon (Vulcan XC-72),4 mg of the prepared sample, 20 μL of Nafion solution (5 wt%), and 380 μL of isopropanol were ultrasonicated to form a homogenous ink, 4 μL of which was dripped onto the glassy carbon with a diameter of 4 mm and dried completely. Thus, the loading was estimated to be 0.2 mg cm$^{-2}$. Similarly, the Pt/C and Ir/C electrodes were made for comparisons by replacing the sample with the commercial 20% Pt/C or Ir/C. A graphite wire and a Hg/HgO electrode were applied as the counter and reference electrodes, respectively, and 0.1 M KOH aqueous solution was used as the electrolyte in the three-electrode system. Linear sweep voltammetry (LSV) at a scan rate of 5 mV s$^{-1}$ was conducted to examine the ORR and OER polarization. For the ORR test, the electrolyte was saturated by oxygen, and the rotation speed changes from 400 to 2500 rpm through a controller (Pine Instrument Co.). For the OER test, the rotation speed of 1600 rpm was used. All potentials were calibrated to a reversible hydrogen electrode (RHE) scale:

$$E_{\mathrm{RHE}} = E_{\mathrm{Hg/HgO}} + 0.059\mathrm{pH} + 0.098 \quad (1)$$

### 2.4 Battery performance

To prepare the air electrode, the catalyst ink composed of 50 wt% catalyst ($Fe_2O_3$/N-rGO or Pt/C), 25 wt% of active carbon, and 25 wt% of polytetrafluoroethylene binder was sprayed onto a gas diffusion layer (Toray TGP-H-060), and the catalyst loading was controlled to be 2 mg $cm^{-2}$. Using the as-prepared air electrode, a Zn foil, and an alkaline electrolyte of 6 M KOH and 0.1 M zinc acetate, a Zn-air battery was assembled. The polarization voltage profiles were obtained using a current step of 1 mA $s^{-1}$. The discharge performance was evaluated at 10 mA $cm^{-2}$, and the capacity was normalized according to the consumed Zn (mAh $g_{Zn}^{-1}$). The discharge-charge cycling stability was tested at 5 mA $cm^{-2}$ with a fixed time interval.

## 3. Results and discussion

### 3.1 Characterization of $Fe_2O_3$/N-rGO

The XRD pattern of $Fe_2O_3$/N-rGO is shown in Fig. 1a. The peaks corresponding to α-$Fe_2O_3$ (JCPDS card No. 33-0664) can be clearly identified, indicating that the α-$Fe_2O_3$ with good crystallinity was successfully synthesized. In addition, the peaks located at around 25°, and 43° can be observed, which are indexed to the N-rGO as previously reported,[25,44] and the weak intensity may be caused by the low contents of graphene in the composition and the decoration of $Fe_2O_3$ nanoparticles. The structural information of $Fe_2O_3$/N-rGO was further confirmed from the Raman spectrum shown in Fig. 1b. Five strong peaks within 200 to 700 $cm^{-1}$ are corresponding to the α-$Fe_2O_3$ phase,[45] and another two peaks at around 1325 and 1600 $cm^{-1}$ are assigned to the characteristic D and G peaks, which indicate the degree of

defects and the in-plane stretching vibration of carbon atom $sp^2$ hybridization, respectively.[46] The ratio of the intensity ($I_D/I_G$) was calculated to be 1.3, indicating a lower crystallinity that may be caused by the N-doping and the growth of $Fe_2O_3$. The addition of $Fe_2O_3$ and more defects in $Fe_2O_3$/N-rGO may be favorable for the oxygen electrocatalysis.[25]

The binding states of $Fe_2O_3$/N-rGO were employed by the XPS characterization. As shown in the survey scan (Fig. 2a), Fe, O, C, and N are all identified, and the weight percentage of N is estimated to be 2.0%. The high-resolution spectrum of Fe 2p in Fig. 2b can be deconvoluted with $Fe^{3+}$ (713.5 and 729.1 eV), $Fe^{2+}$ (710.9 and 724.6 eV), and a satellite peak at 719.2 eV. Although mixed valence states of Fe appear on the sample surface, the evidently distinguished satellite peak (719.2 eV) is a representative fingerprint for $Fe_2O_3$.[47] It is also noticeable that no signal of $Fe^0$ at 707 eV was detected,[26] demonstrating the formation of $Fe_2O_3$ with the absence of $Fe^0$ in the catalyst. For the O 1s spectrum in Fig. 2c, it can be divided into two peaks of $O_{cry}$ and $O_{che}$ at 529.9 and 531.2 eV, respectively, which are assigned to the crystal lattice oxygen and the chemisorbed oxygen, respectively,[42] and the latter one can adsorb oxygen ion to induce the reduction reaction. In this sample, the peak area of $O_{che}$ is 1.55 times of $O_{cry}$, implying high ORR electrocatalytic activity.[48] The C 1s spectrum in Fig. 2d can be divided into four configurations at 284.5, 285.6, 286.5 and 289.8 eV, respectively, which are attributed to C=C in aromatic rings, and C–N, C–O, and O=C–O groups, respectively.[49] Fig. 2e shows the high-resolution N 1s spectrum, which confirms the successfully doping of N, and it can be fitted by three deconvoluted peaks at 398.5 eV (pyridinic N), 400.1 eV (pyrrolic N), and 401.7 eV (graphitic N), respectively. Among them, the pyrrolic N bonding is the dominant type, which can change the spin density and charge

distribution of carbon atoms, improving the ORR activity.[50]

The microstructures of $Fe_2O_3$/N-rGO were examined by TEM. As shown in Fig. 3a, a large number of $Fe_2O_3$ nanoparticles with sizes of around 37 nm are uniformly anchored on the N-rGO sheet surface. This may be attributed to the dissolution-recrystallization of $Fe_2O_3$ in the hydrothermal reaction for the reduction of GO to rGO and the combination of $Fe_2O_3$ nanoparticles with N-rGO. Hence, N-rGO sheets prevent the accumulation of $Fe_2O_3$ nanoparticles and benefit their uniform distribution, which are favorable for utilizing the active surfaces. From the TG analyses, the content of N-rGO in $Fe_2O_3$/N-rGO is calculated to be around 17.82% (Fig. S1), very close to our experimental design ($Fe_2O_3$: 24 mg; GO: 6 mg). Fig. 3b shows the high-resolution image of $Fe_2O_3$ nanoparticles, from which the pores with the diameters of ~5 nm are homogeneously distributed. The inset of Fig. 3b reveals that the interplaner spacing of 0.184 nm in a nanoparticle, which is corresponding to the (024) plane of α-$Fe_2O_3$. Due to the porous structure of $Fe_2O_3$ nanoparticles and the large surface areas provided by the N-rGO sheets, the specific surface area of $Fe_2O_3$/N-rGO is measured to be 41.5 $m^2$ $g^{-1}$, and the mesoporous nature is illustrated by the pore size analysis (Fig. 4), from which the average pore is 3.1 nm. The high surface area and mesoporous structure not only provide abundant active areas between the electrode and the electrolyte, but also facilitate the species transport.

### 3.2 Electrochemical performance

The activity of $Fe_2O_3$/N-rGO, and $Fe_2O_3$, N-rGO, and commercial 20 wt% Pt/C for the ORR was tested in 0.1 M KOH. As the LSV curves shown in Fig. 6a, $Fe_2O_3$ exhibits the lowest onset potential and the highest Tafel slope of 82.6 mV $dec^{-1}$ (Fig. 6b), as well as the

lowest current of 3.58 mA $cm^{-2}$. For N-rGO, the onset potential is much higher than that of $Fe_2O_3$, and the limiting current is 4.62 mA $cm^{-2}$, demonstrating the higher ORR activity. When combining $Fe_2O_3$ and N-rGO to form $Fe_2O_3$/N-rGO, it is interesting to find that the onset potential is close to that of N-rGO, but the Tafel slope is further reduced to 63.4 mV $dec^{-1}$, approximate to that of commercial Pt/C (61.6 mV $dec^{-1}$). In addition, the limiting current increases to 5.01 mA $cm^{-2}$, approaching the value of Pt/C (5.20 mA $cm^{-2}$). This high activity may come from the synergy effects of $Fe_2O_3$ and N-rGO with a reasonable mass ratio. To demonstrate this, we also fabricated $Fe_2O_3$/N-rGO with different weights of GO from 2 to 8 mg, and the electrochemical activity was tested. As shown in Fig. S2a, even at a low mass of 2 mg, the addition of GO remarkably improves the onset potential and current density. When the mass in the fabrication process increases to 6 mg, both the onset potential and the limiting current density improve. However, when further increased to 8 mg, the onset potential and the Tafel slope do not increase any longer; instead, the limiting current density decreases to 4.92 mA $cm^{-2}$. This may be caused by the reason that GO nanosheets start to stack, covering the active sites and thus lead to decreased ORR performance. Hence, using 6 mg of GO in the fabrication process of $Fe_2O_3$/N-rGO leads to the best performance.

Fig. 5c shows the LSV curves of $Fe_2O_3$/N-rGO at different rotation speeds. The current density increases with an increase of the rotation rate, while the onset potential maintains a constant. The relationship between the measured current density ($j$), kinetic current density ($j_k$), and mass transfer correction are expressed by the Koutecky-Levich equation as:

$$j^{-1} = j_k^{-1} + (0.2nFD_{O_2}^{2/3}v^{-1/6}C_{O_2}\omega^{1/2})^{-1} \quad (2)$$

where $n$ is the number of electrons transferred, $F$ is the Faraday constant (96485 C $mol^{-1}$),

$D_{O_2}$ and $C_{O_2}$ is the diffusion coefficient (1.86 × $10^{-5}$ $cm^2$ $s^{-1}$) and the bulk concentration (1.21 × $10^{-6}$ mol $cm^{-3}$) of $O_2$, respectively, $v$ is the kinetic viscosity of the electrolyte (1.01 × $10^{-2}$ $cm^2$ $s^{-1}$), and $\omega$ is the rotation speed (rpm). The corresponding Koutecky-Levich plots in the inset of Fig. 5c show good linearity, indicating the first-order reaction kinetics for the ORR.[42] The number of transferred electrons is calculated to be ~4 at various potentials, illustrating a four-electron process. Moreover, the stability of $Fe_2O_3$/N-rGO during the ORR process was measured by the chronoamperometry measurement at 0.3 V for 20 h. As demonstrated in Fig. 5d, $Fe_2O_3$/N-rGO preserves 86.76% of its initial current density, much higher than commercial Pt/C (79.85%), demonstrating its remarkable stability.

In addition to the ORR performance, the OER activity was also tested, as shown in Fig. 6. For original $Fe_2O_3$ nanoparticles, the OER activity is poor and even lower than that of Pt/C. When decorating $Fe_2O_3$ nanoparticles on N-rGO, an enhanced OER activity is exhibited, and the Tafel slope decreases to 118.2 mV $dec^{-1}$, which is even superior to that of Ir/C. Although lower current densities than Ir/C are observed over a large potential range, the potential for achieving 10 mA $cm^{-2}$ is 1.72 V for $Fe_2O_3$/N-rGO, lower than those of FeCo-N-Carbon (1.73 V) and $IrO_2$ (1.82 V) in the reported work.[51] The improved OER activity may come from the proper ratio of $Fe_2O_3$ and N-rGO, resulting in the best synergy effect (Fig. S2b). Moreover, at the constant current density of 10 mA $cm^{-2}$, $Fe_2O_3$/N-rGO exhibits an increased potential of only 10.7 mV after 5500 min (Fig. S3), demonstrating the remarkable OER stability. Hence, the developed $Fe_2O_3$/N-rGO shows high ORR and OER activity, indicating the potential as a bifunctional electrocatalyst in alkaline solutions (Table S1).[52–56]

### 3.3 Application in Zn-air batteries

The application of $Fe_2O_3$/N-rGO as the catalyst was tested in a home-made Zn-air battery, and compared with that using commercial Pt/C catalyst.[55] Fig. 7a shows the discharge polarization voltage profiles and the corresponding power densities. For the battery with commercial Pt/C, after the activation loss, the discharge voltage decreases linearly with an increase of the current density, and the peak power density of 82.6 mW $cm^{-2}$ is delivered at 135 mA $cm^{-2}$. While for the battery using $Fe_2O_3$/N-rGO, although the discharge voltage is lower than that using Pt/C after the activation, the decrease rate is much lower, which results in a peak power density of 80.1 mW $cm^{-2}$ at 187 mA $cm^{-2}$. This value is approximate to that of Pt/C and also much higher than those of reported $Fe_2O_3$-based catalyst (e.g., NiO-$Fe_2O_3$/carbon nanotube: 13.02 mW $cm^{-2}$).[33] Fig. 7b shows the galvanostatic discharge voltage curves, from which $Fe_2O_3$/N-rGO and Pt/C give the voltage plateaus of 1.05 and 1.12 V, respectively. After the consumption of Zn, the battery with $Fe_2O_3$/N-rGO achieves a capacity of 696.0 mAh $g_{Zn}^{-1}$ and an energy density of 730.2 Wh $kg_{Zn}^{-1}$. In comparison, Pt/C just results in a capacity of 649.5 mAh $g_{Zn}^{-1}$ and an energy density of 721.5 Wh $kg_{Zn}^{-1}$. Hence, a higher capacity and energy density can be achieved by using $Fe_2O_3$/N-rGO.

In addition to the discharge performance, the charge polarization curves were also measured (Fig. S4). Compared to Pt/C, lower charge voltages are exhibited, agrees well with the results shown in Fig. 6. The voltage raises to 2.0 V at 21.4 mA $cm^{-2}$, and reached 2.3 V at 50 mA $cm^{-2}$, indicating the applicability of $Fe_2O_3$/N-rGO for rechargeable Zn-air batteries. To demonstrate this, the discharge-charge stability of $Fe_2O_3$/N-rGO was evaluated by pulse tests at 5 mA $cm^{-2}$, and stable voltages for 120 cycles (40 h) is displayed in Fig. 8a. In comparison, although Pt/C initially results in a high discharge voltage, the voltage gap

gradually increases with cycling. This phenomenon can be explained as follows: although Pt/C demonstrates the higher ORR activity, the stability is insufficient, leading to decreased discharge voltages. Besides, the poor OER activity of Pt/C results in a high charge voltage, which may cause carbon corrosion and further aggregate the performance degradation. Consequently, the discharge and charge voltages keep decreasing and increasing, respectively. By contrast, even though the ORR activity of $Fe_2O_3$/N-rGO is lower than that of Pt/C, the ORR stability is superior (Fig. 5). In addition, higher OER activity (Fig. 6) and stability are exhibited in $Fe_2O_3$/N-rGO. As a result, stable discharge and charge voltages are achieved. For a clear comparison, we selected the middle stages during discharge and charge to measure the voltage gap. As shown in Fig. S5, the voltage gap of $Fe_2O_3$/N-rGO changes from 0.911 V to 0.929 V, with an increase on only 18 mV; while the gap for Pt/C enlarges from 0.801 V to 1.197 V. Based on the energy delivered during discharge and consumed during charge, the energy efficiency for $Fe_2O_3$/N-rGO keeps stable at around 60%, but it decreases from 61% to 47% for Pt/C (Fig. 8b). We also characterized the $Fe_2O_3$/N-rGO electrode after the cycling test. The XRD pattern is shown in Fig. S6a, from which the peaks assigned to $Fe_2O_3$ are well identified, verifying the stability in crystallinity. In addition, as the TEM image shown in Fig. S6b, $Fe_2O_3$ nanoparticles are distributed on the N-rGO surface, similar to the initial morphology. Thus, $Fe_2O_3$/N-rGO can preserve the composition and morphology during the present cycling test. The increased voltage gap in the Zn-air battery may be attributed to the contamination of carbon dioxide on the electrolyte and the passivation on the zinc electrode.[57] Hence, $Fe_2O_3$/N-rGO is demonstrated to be an effective and stable catalyst for rechargeable Zn-air batteries, which is remarkable among recently reported catalysts as listed in Table

S1.[52–56] To further investigate the catalyst degradation mechanism, stable zinc electrode, electrolyte, and testing atmosphere (e.g., in pure oxygen instead of air) should be applied, which is our on-going research topic.

## 4. Conclusions

$Fe_2O_3$ nanoparticle-decorated N-doped reduced graphene ($Fe_2O_3$/N-rGO) has been synthesized in this work, in which porous $Fe_2O_3$ nanoparticles with sizes of ~37 nm are anchored on the N-rGO surface uniformly. In the ORR process, $Fe_2O_3$/N-rGO exhibits a limiting current density of 5.01 mA $cm^{-2}$ and a Tafel slope of 63.4 mV $dec^{-1}$, close to those of commercial Pt/C (5.20 mA $cm^{-2}$, 61.6 mV $dec^{-1}$). In addition, it preserves 86.76% of the initial current density after 20 h, much higher than Pt/C (79.85%). In the OER process, enhanced activity with a Tafel slope of 118.2 mV $dec^{-1}$ and stability is demonstrated. Hence, the developed $Fe_2O_3$/N-rGO shows high ORR and OER activity. Consequently, a Zn-air battery with $Fe_2O_3$/N-rGO delivers a peak power density of 80.1 mW $cm^{-2}$ and an energy density of 730.2 Wh $kg_{Zn}^{-1}$. Moreover, stable charge-discharge voltage gaps of ~0.91 V with the energy efficiency of around 60% for 120 cycles are demonstrated at 5 mA $cm^{-2}$. The results illustrate that $Fe_2O_3$/N-rGO is a promising catalyst for rechargeable Zn-air batteries. To date, the reported highest lifetime for rechargeable Zn-air batteries is 1000 h with over 6000 cycles.[58] As the development of bifunctional catalysts is still in the early stage, the stability standard requires more investigations for commercial implementations.

## Acknowledgments

P. Tan thanks the funding support from CAS Pioneer Hundred Talents Program. M. Ni thanks the funding support from The Hong Kong Polytechnic University (G-YBJN and

G-YW2D), a fund from RISUD (1-ZVEA), and a grant (Project Number: PolyU 152214/17E) from Research Grant Council, University Grants Committee, Hong Kong SAR.

**References**

1. Z. P. Cano , D. Banham, S. Ye, A. Hintennach, J. Lu, M. Fowler, and Z. Chen, *Nat. Energy*, **3**, 279–289 (2018).

2. R. Schmuch, R. Wagner, G. Hörpel, T. Placke, and M. Winter, *Nat. Energy*, **3**, 267–278 (2018).

3. J. Fu, Z.P. Cano, M.G. Park, A. Yu, M. Fowler, and Z. Chen, *Adv. Mater.*, **29**, 1604685 (2017).

4. K.-N. Jung, J. Kim, Y. Yamauchi, M.-S. Park, J.-W. Lee, and J. H. Kim, *J. Mater. Chem. A*, **4**, 14050–14068 (2016).

5. P. Tan, Z. H. Wei, W. Shyy, T. S. Zhao, and X. B. Zhu, *Energy Environ. Sci.*, **9**, 1783–1793 (2016).

6. P. Hartmann, C.L. Bender, M. Vračar, A.K. Dürr, A. Garsuch, J. Janek, and P. Adelhelm, *Nat. Mater.*, **12**, 228–32 (2013).

7. P. Tan, B. Chen, H. Xu, H. Zhang, W. Cai, M. Ni, M. Liu, and Z. Shao, *Energy Environ. Sci.*, **10**, 2056–2080 (2017).

8. Y. Li, and H. Dai, *Chem. Soc. Rev.*, **43**, 5257–5275 (2014).

9. D. U. Lee, P. Xu, Z.P. Cano, A.G. Kashkooli, M.G. Park, and Z. Chen, *J. Mater. Chem. A*, **4**, 7107–7134 (2016).

10. J.-I. Jung, M. Risch, S. Park, M.G. Kim, G. Nam, H.-Y. Jeong, Y. Shao-Horn, and J. Cho, *Energy Environ. Sci.*, **9**, 176–183 (2016).

11. H. A. Gasteiger, S. S. Kocha, B. Sompalli, and F. T. Wagner, *Appl. Catal. B Environ.*, **56**, 9–35 (2005).

12. G. Fu Z. Cui, Y. Chen, L. Xu, Y. Tang, and J. B. Goodenough, *Nano Energy*, **39**, 77–85 (2017).

13. G. Du, X. Liu, Y. Zong, T.S.A. Hor, A. Yu, and Z. Liu, *Nanoscale*, **5**, 4657–4661 (2013).

14. Y. Wang, X. Ma, L. Lu, Y. He, X. Qi, and Y. Deng, *Int. J. Hydrogen Energy*, **38**, 13611–13616 (2013).

15. A. R. Mainar, L.C. Colmenares, O. Leonet, F. Alcaide, J.J. Iruin, S. Weinberger, V. Hacker, E. Iruin, I. Urdanpilleta, and J. A. Blazquez, *Electrochim. Acta*, **217**, 80–91 (2016).

16. M. C. Wu, T. S. Zhao, H. R. Jiang, L. Wei, and Z. H. Zhang, *Electrochim. Acta*, **222**, 1438–1444 (2016).

17. Q. Wang, L. Shang, R. Shi, X. Zhang, Y. Zhao, G.I.N. Waterhouse, L.-Z. Wu, C.-H. Tung, and T. Zhang, *Adv. Energy Mater.*, **7**, 1700467 (2017).

18. P. Tan, B. Chen, H. Xu, W. Cai, W. He, M. Liu, Z. Shao, and M. Ni, *Small*, **14**, 1800225 (2018).

19. J. Yin, Y. Li, F. Lv, Q. Fan, Y.-Q. Zhao, Q. Zhang, W. Wang, F. Cheng, P. Xi, and S. Guo, *ACS Nano*, **11**, 2275–2283 (2017).

20. Z.-F. Huang, J. Wang, Y. Peng, C.-Y. Jung, A. Fisher, and X. Wang, *Adv. Energy Mater.*, **7**, 1700544 (2017).

21. P. Tan, B. Chen, H. Xu, W. Cai, M. Liu, Z. Shao, and M. Ni, *J. Electrochem. Soc.*, **165**, A2119–A2126 (2018).

22. M. Sun, Y. Dong, G. Zhang, J. Qu, and J. Li, *J. Mater. Chem. A*, **2**, 13635–13640 (2014).

23. V. M. Dhavale, S. K. Singh, A. Nadeema, S. S. Gaikwad, and S. Kurungot, *Nanoscale*, **7**, 20117–20125 (2015).

24. T. Zhang, L. Guan, C. Li, J. Zhao, M. Wang, L. Peng, J. Wang, and Y. Lin, *Catalysts*, **8**, 101 (2018).

25. M. Sun, G. Zhang, H. Liu, Y. Liu, and J. Li, *Sci. China Mater.*, **58**, 683–692 (2015).

26. X. Xu, C. Shi, Q. Li, R. Chen, and T. Chen, *RSC Adv.*, **7**, 14382–14388 (2017).

27. H. Zhao, J. Wang, C. Chen, D. Chen, Y. Gao, M. Saccoccio, and F. Ciucci, *RSC Adv.*, **6**, 64258–64265 (2016).

28. M. C. Wu, T. S. Zhao, P. Tan, H. R. Jiang, and X. B. Zhu, *Electrochim. Acta*, **211**, 545–551 (2016).

29. W. Chen, Z. Zhang, W. Bao, Y. Lai, J. Li, Y. Gan, and J. Wang, *Electrochim. Acta*, **134**, 293–301 (2014).

30. C. Gong, L. Zhao, S. Li, H. Wang, Y. Gong, R. Wang, and B. He, *Electrochim. Acta*, **281**, 338–347 (2018).

31. R. Zhang, T. S. Zhao, M. Wu, P. Tan, and H. Jiang, *Energy Technol.*, **6**, 263–272 (2018).

32. Z. Li, S. Ganapathy, Y. Xu, Q. Zhu, W. Chen, I. Kochetkov, C. George, L.F. Nazar, and M. Wagemaker, *Adv. Energy Mater.*, **0**, 1703513 (2018).

33. J. Fang, L. Hu, M. Wang, L. Gan, C. Chen, Y. Jiang, B. Xiao, Y. Lai, and J. Li, *Mater. Lett.*, **218**, 36–39 (2018).

34. Y. Zang, H. Zhang, X. Zhang, R. Liu, S. Liu, G. Wang, Y. Zhang, and H. Zhao, *Nano Res.*, **9**, 2123–2137 (2016).

35. N. Mahmood, C. Zhang, H. Yin, and Y. Hou, *J. Mater. Chem. A*, **2**, 15–32 (2014).

36. Q. Wang, Y. Lei, Z. Chen, N. Wu, Y. Wang, B. Wang, and Y. Wang, *J. Mater. Chem. A*, **6**, 516–526 (2018).

37. Q. Li, N. Mahmood, and J. Zhu, *Nano Today*, **9**, 668–683 (2014).

38. H. R. Jiang, P. Tan, M. Liu, Y. K. Zeng, and T. S. Zhao, *J. Phys. Chem. C*, **120**, 18394–18402 (2016).

39. H. R. Jiang, T. S. Zhao, L. Shi, P. Tan, and L. An, *J. Phys. Chem. C*, **120**, 6612–6618 (2016).

40. L. L. Tian, J. Yang, M.Y. Weng, R. Tan, J.X. Zheng, H.B. Chen, Q.C. Zhuang, L.M. Dai, and F. Pan, *ACS Appl. Mater. Interfaces*, **9**, 7125–7130 (2017).

41. B. J. Kim, D.U. Lee, J. Wu, D. Higgins, A. Yu, and Z. Chen, *J. Phys. Chem. C*, **117**, 26501–26508 (2013).

42. K. Liu, J. Li, Q. Wang, X. Wang, D. Qian, J. Jiang, J. Li, and Z. Chen, *J. Alloys Compd.*, **725**, 260–269 (2017).

43. A. Lassoued, B. Dkhil, A. Gadri, and S. Ammar, *Results Phys.*, **7**, 3007–3015 (2017).

44. M. Khan, A.H. Al-Marri, M. Khan, M.R. Shaik, N. Mohri, S.F. Adil, M. Kuniyil, H.Z. Alkhathlan, A. Al-Warthan, W. Tremel, M.N. Tahir, and M. R. H. Siddiqui, *Nanoscale Res. Lett.*, **10**, 1–9 (2015).

45. J. Krysa, M. Zlamal, S. Kment, M. Brunclikova, and Z. Hubicka, *Molecules*, **20**, 1046–1058 (2015).

46. L. Wang, J. Yin, L. Zhao, C. Tian, P. Yu, J. Wang, and H. Fu, *Chem. Commun.*, **49**, 3022–3024 (2013).

47. J. Zhu, L. Li, Z. Xiong, Y. Hu, and J. Jiang, *ACS Sustain. Chem. Eng.*, **5**, 269–276 (2017).

48. J. Hu, L. Wang, L. Shi, and H. Huang, *Electrochim. Acta*, **161**, 115–123 (2015).

49. N. Zhou, Q. An, Z. Xiao, S. Zhai, and Z. Shi, *RSC Adv.*, **7**, 45156–45169 (2017).

50. H. Wang, T. Maiyalagan, and X. Wang, *ACS Catal.*, **2**, 781–794 (2012).

51. C.-Y. Su, H. Cheng, W. Li, Z.-Q. Liu, N. Li, Z. Hou, F.-Q. Bai, H.-X. Zhang, and T.-Y. Ma, *Adv. Energy Mater.*, **7**, 1602420 (2017).

52. Y. Qiao, P. Yuan, Y. Hu, J. Zhang, S. Mu, J. Zhou, H. Li, H. Xia, J. He, and Q. Xu, *Adv. Mater.*, **30**, 1–9 (2018).

53. L. Wei, H.E. Karahan, S. Zhai, H. Liu, X. Chen, Z. Zhou, Y. Lei, Z. Liu, and Y. Chen, *Adv. Mater.*, **29**, 1–10 (2017).

54. X. Qin, Z. Wang, J. Han, Y. Luo, F. Xie, G. Cui, X. Guo, and X. Sun, *Chem. Commun.*, **54**, 7693–7696 (2018).

55. S. Han, X. Hu, J. Wang, X. Fang, and Y. Zhu, *Adv. Energy Mater.*, **8**, 1800955 (2018).

56. H. B. Yang, J. Miao, S.-F. Hung, J. Chen, H.B. Tao, X. Wang, L. Zhang, R. Chen, J. Gao, H.M. Chen, L. Dai, and B. Liu, *Sci. Adv.*, **2**, e1501122–e1501122 (2016).

57. P. Tan, B. Chen, H. Xu, W. Cai, W. He, and M. Ni, *Appl. Catal. B Environ.*, **241**, 104–112 (2019).

58. S. S. Shinde, C.H. Lee, J.-Y. Jung, N.K. Wagh, S.-H. Kim, D.-H. Kim, C. Lin, S.U. Lee, and J.-H. Lee, *Energy Environ. Sci.* DOI: 10.1039/c8ee02679c (2019).

**Figure captions**

**Fig. 1** Characterization of $Fe_2O_3$/N-rGO. (a) XRD pattern and (b) Raman spectrum.

**Fig. 2** XPS analyses of $Fe_2O_3$/N-rGO. (a) Full survey, (b) Fe 2p, (c) O 1s, (d) C 1s, and (e) N 1s.

**Fig. 3** TEM images of $Fe_2O_3$/N-rGO. (a) Low-resolution image, and the inset shows the particle size distribution of $Fe_2O_3$. (b) High-resolution image to show the pores in $Fe_2O_3$ particles, and the inset shows the interplaner spacing of a $Fe_2O_3$ particle.

**Fig. 4** Nitrogen adsorption-desorption isotherm of $Fe_2O_3$/N-rGO, the inset shows the pore size distribution.

**Fig. 5** Electrochemical activity toward the ORR in the $O_2$-saturated 0.1 M KOH electrolyte. (a) LSV curves of $Fe_2O_3$, N-rGO, $Fe_2O_3$/N-rGO, and Pt/C at a scan rate of 5 mV $s^{-1}$ and a rotation rate of 1600 rpm. (b) The corresponding Tafel plots. (c) RDE curves at rotating rates ranging from 400 to 2500 rpm, the inset shows the corresponding Koutecky-Levich plots. (d) Chronoamperometric response at a constant potential of 0.30 V (vs. RHE).

**Fig. 6** Electrochemical activity toward the OER in 0.1 M KOH electrolyte. (a) LSV curves of $Fe_2O_3$, N-rGO, $Fe_2O_3$/N-rGO, Pt/C, and Ir/C at a scan rate of 5 mV $s^{-1}$ and a rotation rate of 1600 rpm. (b) The corresponding Tafel plots.

**Fig. 7** Electrochemical performance of Zn-air batteries with $Fe_2O_3$/N-rGO and Pt/C. (a) Polarization curves and corresponding power densities in the ambient air. (b) Discharge voltage profiles at 10 mA $cm^{-2}$.

**Fig. 8** Cycling performance of Zn-air batteries with $Fe_2O_3$/N-rGO and Pt/C. (a) Cycling stability test at a discharge current density of 5 mA $cm^{-2}$ for 10 min discharge and 10 min charge. (b) Energy efficiency as a function of cycle number.

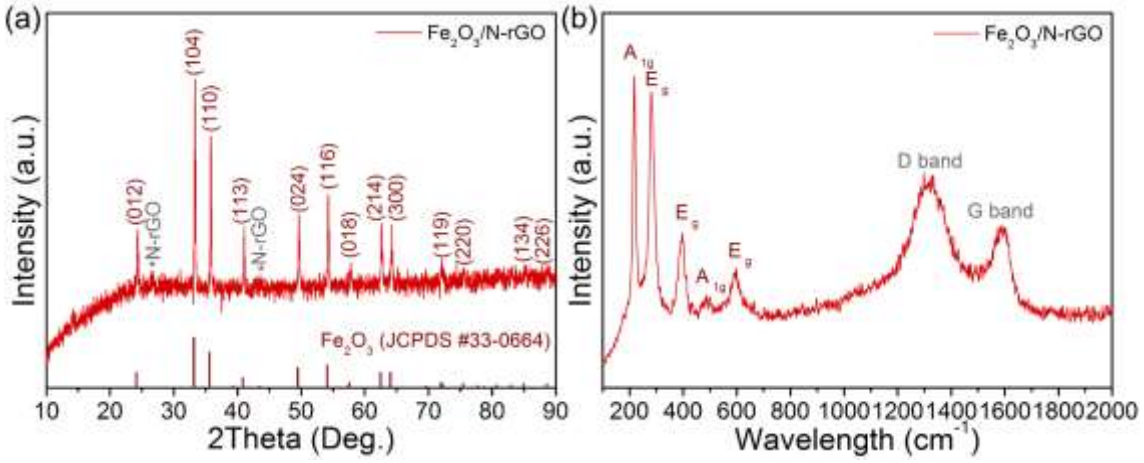


**Fig. 1** Characterization of $Fe_2O_3$/N-rGO. (a) XRD pattern and (b) Raman spectrum.

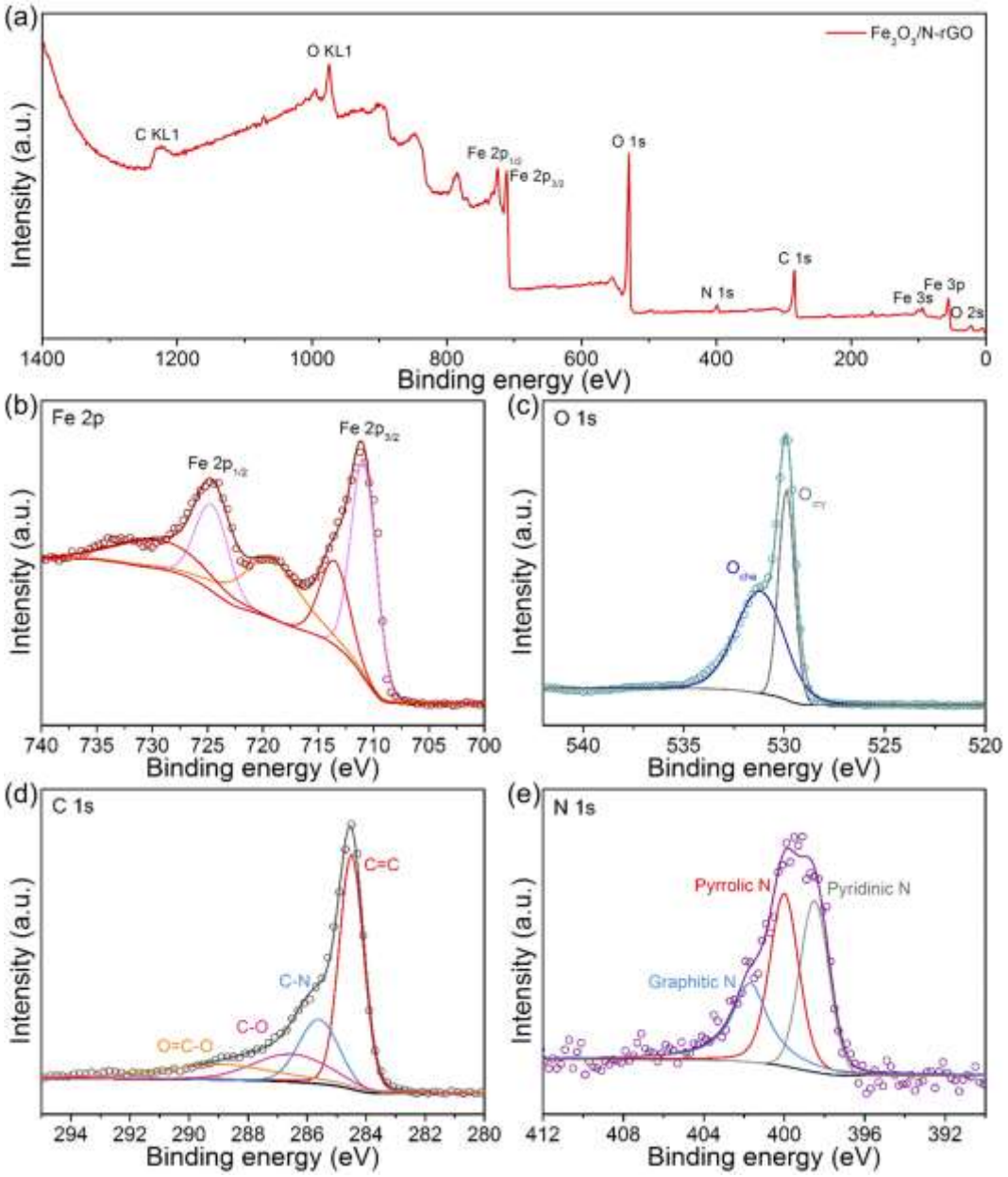


**Fig. 2** XPS analyses of $Fe_2O_3$/N-rGO. (a) Full survey, (b) Fe 2p, (c) O 1s, (d) C 1s, and (e) N 1s.

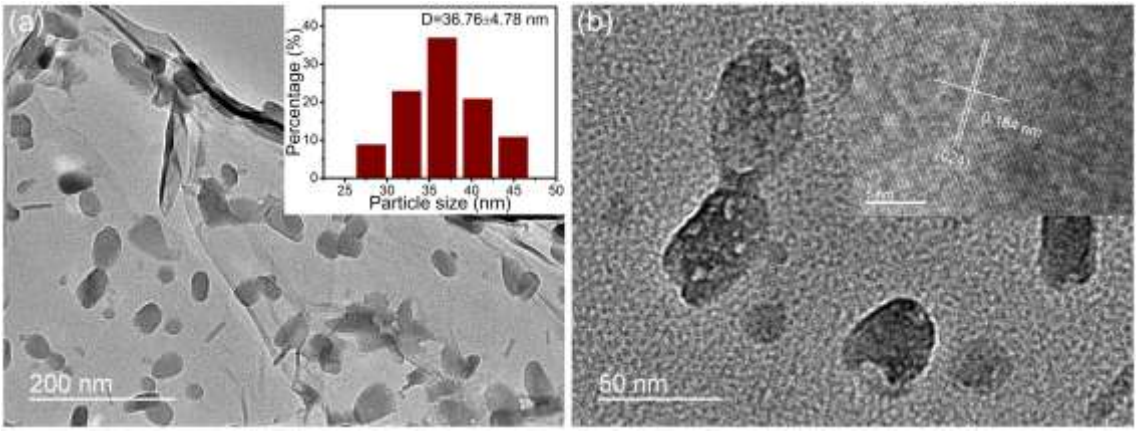


**Fig. 3** TEM images of $Fe_2O_3$/N-rGO. (a) Low-resolution image, and the inset shows the particle size distribution of $Fe_2O_3$. (b) High-resolution image to show the pores in $Fe_2O_3$ particles, and the inset shows the interplaner spacing of a $Fe_2O_3$ particle.

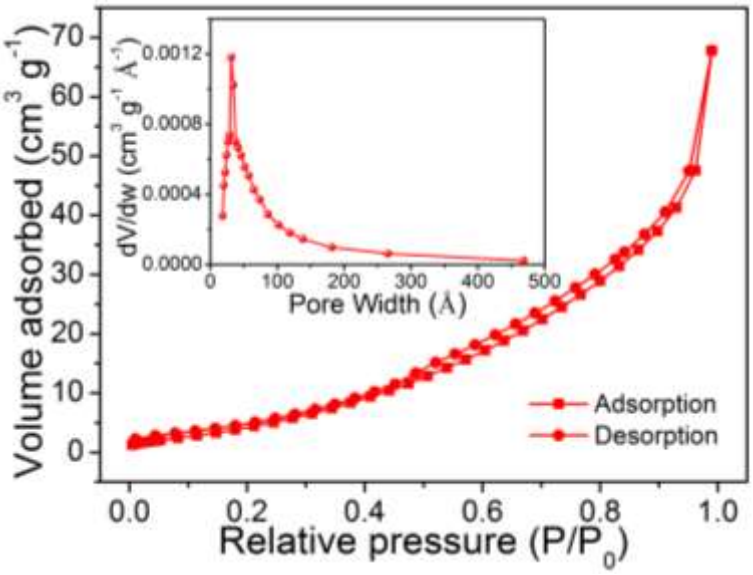


**Fig. 4** Nitrogen adsorption-desorption isotherm of $Fe_2O_3$/N-rGO, the inset shows the pore size distribution.

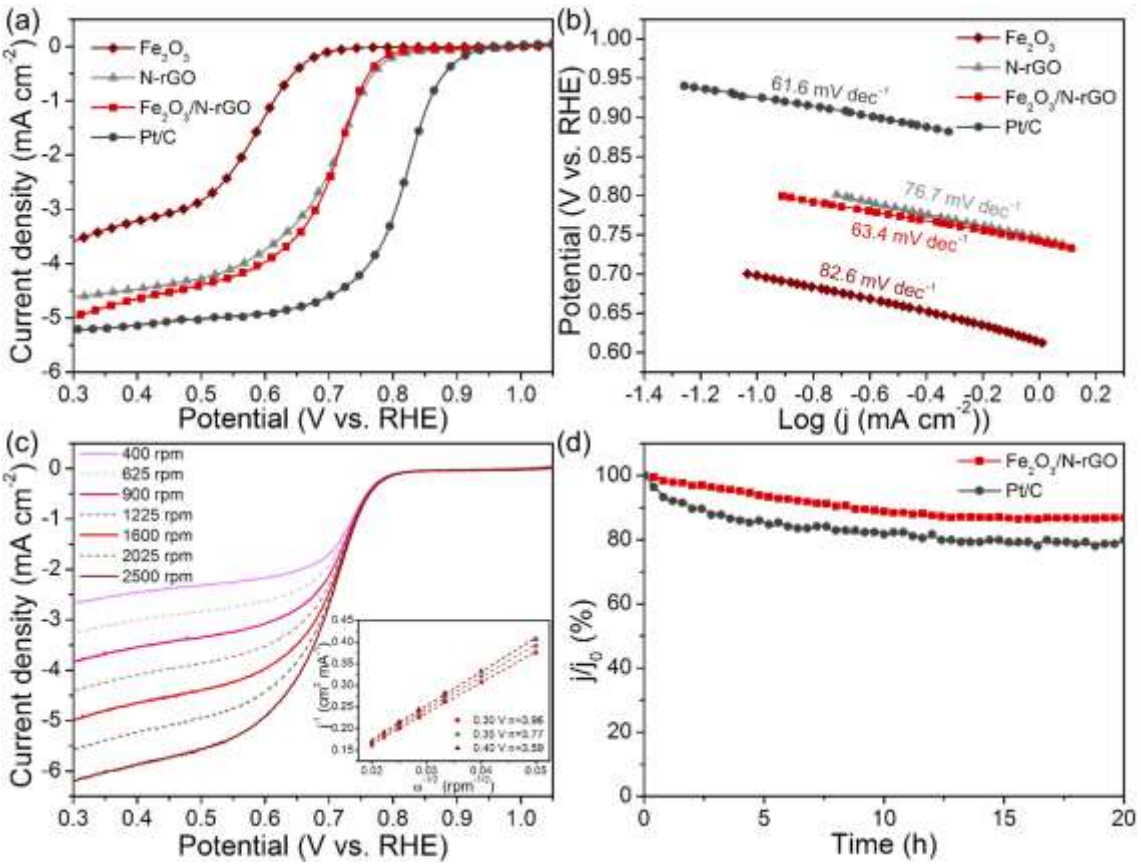


**Fig. 5** Electrochemical activity toward the ORR in the $O_2$-saturated 0.1 M KOH electrolyte. (a) LSV curves of $Fe_2O_3$, N-rGO, $Fe_2O_3$/N-rGO, and Pt/C at a scan rate of 5 mV $s^{-1}$ and a rotation rate of 1600 rpm. (b) The corresponding Tafel plots. (c) RDE curves at rotating rates ranging from 400 to 2500 rpm, the inset shows the corresponding Koutecky-Levich plots. (d) Chronoamperometric response at a constant potential of 0.30 V (vs. RHE).

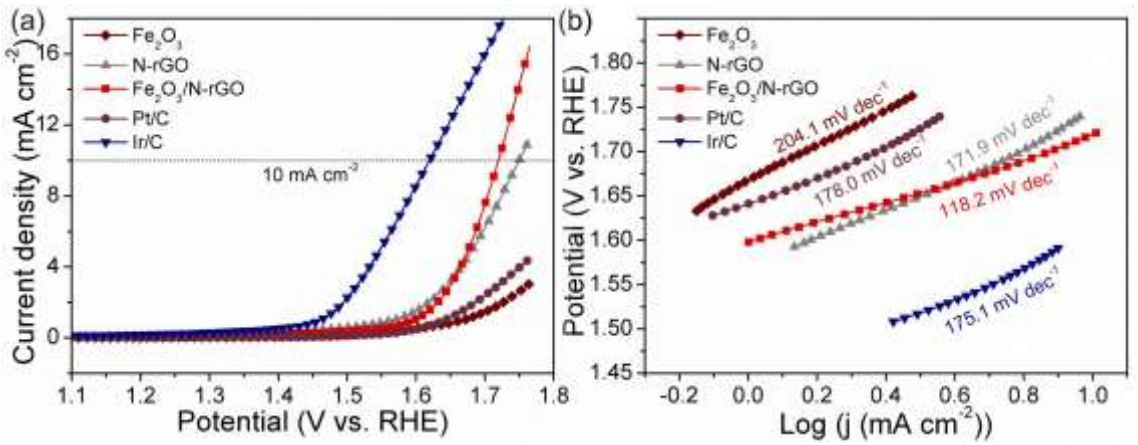


**Fig. 6** Electrochemical activity toward the OER in 0.1 M KOH electrolyte. (a) LSV curves of $Fe_2O_3$, N-rGO, $Fe_2O_3$/N-rGO, Pt/C, and Ir/C at a scan rate of 5 mV $s^{-1}$ and a rotation rate of 1600 rpm. (b) The corresponding Tafel plots.

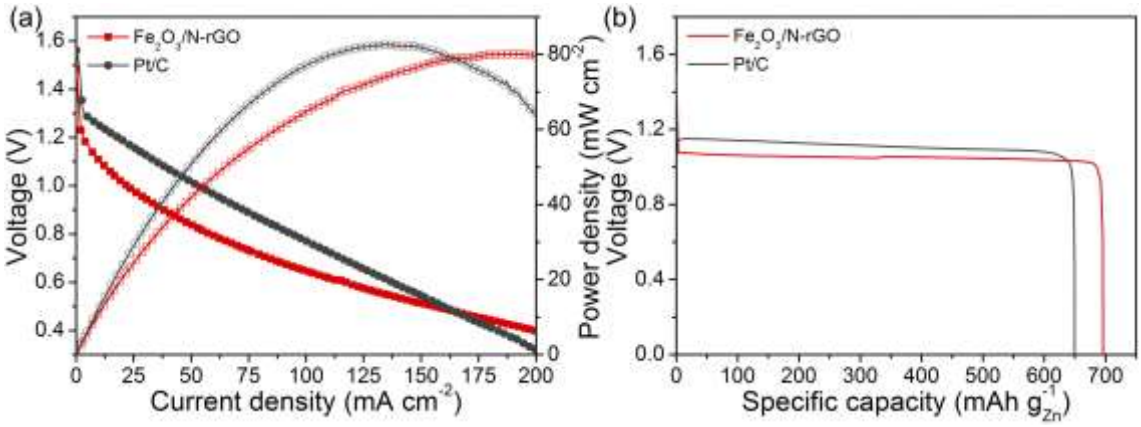


**Fig. 7** Electrochemical performance of Zn-air batteries with $Fe_2O_3$/N-rGO and Pt/C. (a) Polarization curves and corresponding power densities in the ambient air. (b) Discharge voltage profiles at 10 mA $cm^{-2}$.

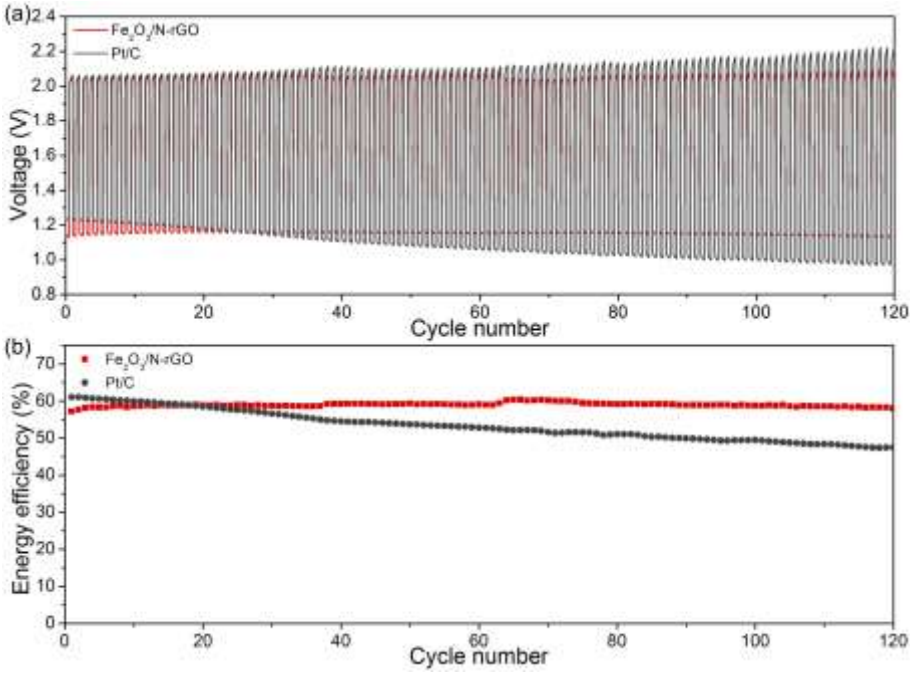


**Fig. 8** Cycling performance of Zn-air batteries with $Fe_2O_3$/N-rGO and Pt/C. (a) Cycling stability test at a discharge current density of 5 mA $cm^{-2}$ for 10 min discharge and 10 min charge. (b) Energy efficiency as a function of cycle number.